Tellus SERIES A DYNAMIC METEOROLOGY AND OCEANOGRAPHY
PUBLISHED BY THE INTERNATIONAL METEOROLOGICAL INSTITUTE IN STOCKHOLM

Tellus (2011), 63A, 939–957
Printed in Singapore. All rights reserved

TELLUS

Application of conditional non-linear optimal perturbations to tropical cyclone adaptive observation using the Weather Research Forecasting (WRF) model

By HONGLI WANG[1]*, MU MU[2] and XIANG-YU HUANG[1], [1]*National Center for Atmospheric Research†, P.O. Box 3000, Boulder, Colorado, 80307, USA;* [2]*Key Laboratory of Ocean Circulation and Waves, Institute of Oceanology, Chinese Academy of Sciences, Qingdao, Shandong, China*

(Manuscript received 19 April 2011; in final form 28 June 2011)

ABSTRACT

Conditional non-linear optimal perturbation (CNOP), which is a natural extension of the linear singular vector into the non-linear regime, has been suggested to identify data-sensitive regions in the adaptive observation strategy. CNOP is the global maximum of a cost function, whereas, local CNOP is the local maximum of the cost function if the local maximum exists. The potential application of CNOPs to tropical cyclone adaptive observation is researched. The CNOPs and the first singular vector (FSV) are numerically obtained by a spectral projected gradient algorithm with the Weather Research Forecasting (WRF) model. This paper examines two tropical cyclone cases, a fast straight moving typhoon Matsa (2005) and a slow moving recurving typhoon Shanshan (2006). The CNOPs and FSVs are obtained using the norms of background error at initial time and total dry energy at final time with a 36-h optimization time interval. The spatial structures of CNOPs, their energies, non-linear evolutions and impacts on track simulations are compared with those of the FSVs. The results show that both the CNOPs and the FSVs are localized, and evolve into the verification area at the final time with the upscale growth of perturbations. However, the CNOPs are different from the FSVs in spatial patterns, wind maximum distribution, growth rate of energy and impact on track simulation. Compared to FSV, CNOP and local CNOP have greater impact on the forecast in the verification region at the final time in terms of total energy, and have larger, at least similar impact on track simulation too. This indicates the CNOP method with constraint of the norm of background error at initial time and total energy norm at final time is a reasonable candidate in tropical cyclone adaptive observation. Therefore, both CNOP and local CNOP are suggested to be considered in tropical cyclone adaptive observation.

1. Introduction

Targeted observing is regarded as an effective way to improve the numerical weather forecasts skill of severe weather events that can have large societal or economic impact. Most studies showed that adaptive observations could produce average forecast error reductions of about 10% over the verification area (Langland, 2005). In certain cases, short-range forecast error reductions up to 50% were obtained (Langland and Rohaly, 1996; Langland, 2005; Montani et al., 2006). For the tropical cyclones during the synoptic surveillance missions, the assimilation of only a subset of data from fully sampled target regions produced a statistically significant reduction of the track forecast errors up to 25% for the 2-d forecast (Aberson, 2003). For Hurricane Humberto (2001), forecasts from two dynamical hurricane track forecast models were improved substantially during the watch and warning period before a projected landfall by the assimilation of the additional dropwindsonde data (Aberson and Etherton, 2006). It was shown that during tropical cyclone activity, and particularly the transition from tropical cyclone to extratropical characteristics, removing observations in sensitive regions, indicated by singular vectors (SVs) optimized on the 2-d forecast over Europe, degraded the accuracy of the forecast more than excluding observations in randomly selected regions (Cardinali et al., 2007). In the typhoon surveillance program Dropwindsonde Observations for Typhoon Surveillance near the Taiwan Region (DOTSTAR), by assimilation of dropwindsonde observations, the mean track error reductions were about 15% in the first 72 forecast hours (Wu et al., 2007a).

However, for certain cases, targeted observations had only neutral or even negative impact on the forecasts (Langland, 2005). Among the factors leading to the negative forecasts, two

*Corresponding author
e-mail: hlwang@ucar.edu
†The National Center for Atmospheric Research is sponsored by the National Science Foundation.
DOI: 10.1111/j.1600-0870.2011.00536.x

possible reasons are: (1) the mismatch of the sensitive area with the 'true' sensitive area and (2) the consistency of the data assimilation system with the forecast model (Langland, 2005).

The first issue listed earlier is directly related to the method used in adaptive observation strategy identifying the sensitive areas where additional observations are expected to improve the analysis and reduce forecast error. Currently, two main strategies have been proposed and applied to identify the sensitive areas. One strategy is based on the adjoint technique, such as the average key analysis error method (Gustafsson and Huang, 1996), SV method (Palmer et al., 1998), adjoint sensitivity method (Langland and Rohaly, 1996; Rabier et al., 1996) and the method based on adjoint-derived sensitivity steering vectors (ADSSV; Wu et al., 2007b). The other strategy is ensemble based. For example, the ensemble transform method (Bishop and Toth, 1999), the ensemble Kalman filter (Hamill and Snyder, 2002) and the ensemble transform Kalman filter (ETKF; Bishop et al., 2001). It should be noted that the above two strategies are based on linear theory. Other methodologies, such as the quasi-inverse linear method (Pu and Kalnay, 1999), the breeding-like method (Lorenz and Emanuel, 1998) and the technique based on deep-layer mean (DLM) wind variance (Aberson, 2003) have also been suggested.

The comparison of targeted observation guidance for tropical cyclones in the Atlantic and the northwestern Pacific Ocean was conducted in previous studies. Majumdar et al. (2006) made a comparison of adaptive observation guidance for Atlantic tropical cyclones, based on total energy SVs and ETKF or DLM wind variance. For major hurricanes, all techniques usually indicated targets close to the storm centre. However, they found that for weaker tropical cyclones, the SV guidance selected similar targets to those from the ETKF (DLM wind variance) in only 30% (20%) of the cases. ETKF guidance, using the ECMWF ensemble, was more like that provided by the National Centers for Environmental Prediction (NCEP) ensemble (and DLM wind variance) for major hurricanes than for weaker tropical cyclones. Wu et al. (2009a) compared six different guidance products for the targeted observations over the northwest Pacific Ocean for some cases in 2006. It was shown that the SVs with total energy norm from ECMWF, Navy Operational Global Atmospheric Prediction System (NOGAPS) and Japan Meteorological Agency (JMA) are relatively similar to one another in both the large and the small domains whereas the comparisons of the DLM wind variance with other methods showed rather little similarities.

In addition to the methods mentioned earlier, a new nonlinear method named conditional non-linear optimal perturbation (CNOP) has been suggested to determine data-sensitive areas in adaptive observations for mesoscale and tropical cyclone forecasts (Mu et al., 2007, 2009). CNOP was obtained by using the fifth-generation Pennsylvania State University, National Center for Atmospheric Research Mesoscale Model (MM5; Grell et al., 1995), its tangent linear and adjoint models in the MM5–4DVAR system (Zou et al., 1997). Results from three tropical cyclone cases (Mu et al., 2009, hereafter MZW2009) indicated that the structures of CNOP differed much from those of first singular vector (FSV) depending on the constraint, the metric and the basic state. The CNOP-type errors had larger impact on the forecasts in the verification area as well as on tropical cyclones than the FSV-type errors. This suggested that the forecast skill was expected to improve from the reduction of CNOP-type error in initial conditions more than FSV-type for mesoscale rainfall and tropical cyclone prediction.

Considering the Advanced Research WRF (ARW) model (Skamarock et al., 2008) and its three- and four-dimensional variational data assimilation system (WRF-3/4DVAR; Barker et al., 2005; Huang et al., 2009) have been used extensively for the atmospheric research and forecasting, we construct the CNOP–FSV optimization system based on components in the WRF-4DVAR system in this paper. This research advances the previous work (MZW2009) to the application of CNOP method into tropical cyclone targeting in the following aspects: (1) The WRF model is used as the dynamical constraint forward model; (2) The background error statistics norm is employed at initial time; (3) The role of local CNOP is further illustrated; (4) The impact of various perturbations on tropical cyclone track is presented and (5) Spectral evolution of various perturbations is shown.

The WRF is the next generation mesoscale model designed to serve both operational forecasting and atmospheric research applications. The ARW model (Skamarock et al., 2008) and its WRF-3/4DVAR data assimilation system have been used extensively in the research community and operational centres. The tangent linear and adjoint models of WRF have been developed and tested in adjoint sensitivity and WRF-4DVAR data assimilation studies (Xiao et al., 2008; Huang et al., 2009; Zhang et al., 2010; Wang et al., 2011). Compared with the MM5–4DVAR system, the WRF-4DVAR system has advanced dynamics, and a more realistic background error covariance matrix. These allow for more realistic constraints at the initial time to obtain the CNOPs for real-time operational targeting and atmospheric predictability studies.

The background error covariance metric is a reasonable choice for the adaptive observation. The benefit of employing a background error covariance is that the statistical uncertainty in the background field is also considered. As a result, in addition to including the model dynamics, the CNOP represents the structure that is likely to happen statistically as well. Additional benefit is that the WRF model and the same background error statistics are used both in the targeting method and the WRF-4DVAR system. This can avoid the mismatch among the targeting method, the data assimilation system and the forecast model, which is one reason that causes targeted observation sometimes to have only neutral or even negative impact on the forecasts. The use of WRF-4DVAR with additional observations in a CNOP region is expected to reduce the initial condition error efficiently.

The role of local CNOP in tropical cyclone targeting was not thoroughly studied in the previous work of MZW2009. The CNOP is the global maximum of a cost function, whereas, local CNOP is the local maximum of the cost function if the local maximum exists (Mu and Zhang, 2006). In adaptive observation study for mesoscale weather system, it was found that the total energy of local CNOP at final time is larger than FSV (Mu et al., 2007), suggesting its important role in targeting. As for its role in tropical cyclone targeting, the local CNOP was found in one tropical cyclone case, and its structure and total energy evolution were studied in MZW2009. In this research, the local CNOP is found in two cases, the structures of local CNOP, its evolution and its impact on tropical cyclone track simulation are also examined as well.

The total energy norm is not an index that related directly to the typhoon movement. Hence, when focusing on tropical cyclone predictions, one may raise the question: 'Is the total energy norm a reasonable candidate of CNOP to improve the tropical cyclone track forecast?' In the previous work of MZW2009, the impact of various perturbations on track simulation was not studied; it is examined in this research. The CNOP (local CNOP) and FSV are obtained numerically by solving a constraint large-scale optimization problem using the spectral projected gradient 2 algorithm (SPG2; Birgin et al., 2001). The spatial structures of the CNOP (local CNOP), their energy and their non-linear evolutions are compared with those of the FSV. The impact of perturbations on tropical cyclone track simulation is studied.

The structure of this paper is arranged as follows: Section 2 introduces CNOP and FSV method; Section 3 briefly describes the model and the experiment design. A comparison of the CNOPs and FSVs at initial time is presented in Section 4. The differences between the evolution of (local) CNOPs and FSVs, including their impact on tropical cyclone track simulation are described in Section 5. The final section provides a summary and discussion.

2. The Methods: CNOP and FSV

The readers are referred to MZW2009 for detailed definitions of CNOP and FSV. Here, we focus on the introduction of background norm in CNOP formulation and the concept of local CNOP. The necessary descriptions are as follows.

2.1. CNOP

Suppose we have the following non-linear differential equations:

$$\begin{cases} \dfrac{\partial \mathbf{x}}{\partial t} + F(\mathbf{x}) = 0 \\ \mathbf{x}|_{t=0} = \mathbf{x_0} \end{cases}, \tag{1}$$

where $\mathbf{x}$ is the state vector of the model with initial value $\mathbf{x_0}$. F is a non-linear partial differential operator. The solution of (1) describes how variables $\mathbf{x}$ evolve in time and can be expressed in discrete form.

$$\mathbf{x}(t) = M(\mathbf{x_0}), \tag{2}$$

where M is a non-linear propagator, $\mathbf{x_0}$ is the initial value vector and $\mathbf{x}(t)$ is the value of $\mathbf{x}$ at time t.

The problem we want to solve is to find an optimal perturbation $\boldsymbol{\delta}\mathbf{x}_0^*$ that satisfies

$$J(\boldsymbol{\delta}\mathbf{x}_0^*) = \max_{\boldsymbol{\delta}\mathbf{x}_0^{\mathrm{T}}\mathbf{C}_1\boldsymbol{\delta}\mathbf{x}_0 \le \beta} J(\boldsymbol{\delta}\mathbf{x_0}), \tag{3}$$

where

$$J(\boldsymbol{\delta}\mathbf{x_0}) = (M(\mathbf{x_0} + \boldsymbol{\delta}\mathbf{x_0}) - M(\mathbf{x_0}))^{\mathrm{T}}\mathrm{C}_2(M(\mathbf{x_0} + \boldsymbol{\delta}\mathbf{x_0}) - M(\mathbf{x_0})).$$

From eq. (3), it is easy to see that $\boldsymbol{\delta}\mathbf{x}_0^*$ has the maximum cost function at time t. $M(\mathbf{x_0} + \boldsymbol{\delta}\mathbf{x_0}) - M(\mathbf{x_0})$is called the non-linear evolution of perturbation $\boldsymbol{\delta}\mathbf{x_0}$. During the optimization period, the different norms, $\mathbf{C_1}$ and $\mathbf{C_2}$ can be used at the initial and final time, respectively.

If the inverse of the background error matrix $\mathbf{B}$ is adopted at initial time, then

$$\boldsymbol{\delta}\mathbf{x}_0^{\mathbf{T}}\mathbf{C_1}\boldsymbol{\delta}\mathbf{x_0} = \boldsymbol{\delta}\mathbf{x}_0^{\mathbf{T}}\mathbf{B^{-1}}\boldsymbol{\delta}\mathbf{x_0}. \tag{4}$$

The background error covariance matrix is of rather huge dimension, its typical size being of $10^6 \times 10^6$ elements. This is not easy to handle either from the viewpoint of memory storage requirements or from that of available statistical information. In WRF-4DVAR system, the transformation from control space to analysis space is used to handle the background error covariance matrix.

Let

$$\mathbf{B} = \mathbf{U}\mathbf{U}^{\mathbf{T}}, \quad \boldsymbol{\delta}\mathbf{x} = \mathbf{U}\mathbf{v}, \tag{5}$$

$$\boldsymbol{\delta}\mathbf{x}_0^{\mathbf{T}}\mathbf{B^{-1}}\boldsymbol{\delta}\mathbf{x} = \mathbf{v}^{\mathbf{T}}\mathbf{v} \le \beta, \tag{6}$$

where $\mathbf{v}$ is control variable. The $\mathbf{U}$ transform is designed to non-dimensionalize the variational problem, and also permit use of filtering techniques that approximate the full background error covariance matrix $\mathbf{B}$.

Then, (3) may be rewritten

$$J(\mathbf{v}^*) = \max_{\mathbf{v}^{\mathbf{T}}\mathbf{v} \le \beta} J(\mathbf{v}) \tag{7}$$

$$J(\mathbf{v}) = (M(\mathbf{x_0} + \mathbf{U}\mathbf{v}) - M(\mathbf{x_0}))^T\mathbf{C_2}(M(\mathbf{x_0} + \mathbf{U}\mathbf{v}) - M(\mathbf{x_0})).$$

In this paper, where $\mathbf{C_2}$ is total dry energy in a continuous expression

$$\boldsymbol{\delta}\mathbf{x}_{\mathbf{t}}^{\mathbf{T}}\mathbf{C_2}\boldsymbol{\delta}\mathbf{x} = \frac{1}{D}\int_D\int_0^1 \left(u'^2 + v'^2 + \frac{C_p}{T_r}T'^2 + R_aT_r\left(\frac{P_s'}{\mathrm{Pr}}\right)^2\right)\mathrm{d}\eta\mathrm{d}D, \tag{8}$$

where c_p and R_a are the specific heat at constant pressure and the gas constant of dry air, respectively (with numerical values

of 1005.7 J kg^{-1} K^{-1} and 287.04 J·kg^{-1}·K^{-1}). T_r (with value of 270 K) and p_r (with value of 1000 hPa) are the reference temperature and pressure, u', v', T' and P_s' are the perturbed zonal and meridional horizontal wind components, temperature and surface pressure, respectively. The integration extends over the verification domain D and the vertical direction η. The vertical coordinate in the WRF model is defined as $\eta = (p_h - p_{ht})/u$, where $u = p_{hs} - p_{ht}$. p_h is the hydrostatic component of the pressure, and p_{hs} and p_{ht} refer to values along the surface and top boundaries, respectively. η varies from a value of 1 at the surface to 0 at the model top.

The non-linear maximum optimization problem is transformed into a minimization problem by defining the cost function

$$J(\mathbf{v}^*) = -\min_{\mathbf{v}^\mathbf{T}\mathbf{v}\le\beta} J(\mathbf{v}) \tag{9}$$

$$J(\mathbf{v}) = (\mathbf{P}S_2(M(\mathbf{x_0} + S\mathbf{U}\mathbf{v}) - M(\mathbf{x_0})))^T \times \mathbf{C_2}(\mathbf{P}S_2(M(\mathbf{x_0} + S\mathbf{U}\mathbf{v}) - M(\mathbf{x_0}))),$$

where M is the non-linear WRF model, S represents the operator mapping the variables from analysis space to model space and S_2 represents the operator mapping the variables from model space to the space the energy norm needs to be calculated. $\mathbf{P}$ is the local projection operator for targeting purpose.

2.2. Local CNOP

Mathematically, CNOP is the global maximum of eq. (1). However, eq. (1) defines a large dimension constrained non-linear optimization problem. It is not straightforward that an optimal solution of such a problem is unique. In some cases, a possibility exists that J has local maximum in a small neighbourhood of a particular point in phase space. Such kind of initial perturbation is called the local CNOP (Mu and Zhang, 2006). Local CNOPs were found in simple and complicated regional models (Mu and Duan, 2003; Duan et al., 2004; Mu and Zhang, 2006; Mu et al., 2007). In some physical problems, the CNOP and the local CNOP possessed clear physical meanings. For example, in the El Niño/Southern Oscillation (ENSO) predictability study, the CNOP (local CNOP) had the physical meaning leading to the El Niño (La Niña) event (Duan et al., 2004). In an adaptive observation study, it was found that the total energy of local CNOP at final time was larger than FSV (Mu et al., 2007, 2009), which indicated it could play an important role in targeting.

2.3. FSV

Suppose that the linear assumption is valid when the initial perturbation is sufficiently small and with a short-term time interval. Then,

$$M(\mathbf{x_0} + S\mathbf{U}\mathbf{v}) - M(\mathbf{x_0}) \approx L(S\mathbf{U}\mathbf{v}). \tag{10}$$

Then, the FSV solves the maximum of the following cost function:

$$J(\mathbf{v}) = (\mathbf{P}S_2L(S\mathbf{U}\mathbf{v}))^T\mathbf{C_2}(\mathbf{P}S_2L(S\mathbf{U}\mathbf{v})), \tag{11}$$

where L is the forward tangent propagator.

The difference between the CNOP and FSV depends on the validation of tangent linear assumption. For example, when the initial constraint is very small and the linear assumption is valid, the CNOP and FSV may have almost the same structure; see Figs 2a and b in MZW2009. However, our interest is in the difference caused by two methods when the initial perturbation has the amplitude of the current analysis or background error, and has a longer optimization time interval as well.

In a previous study of application of CNOP to adaptive observation (Mu et al., 2007, 2009), an iterative optimization algorithm SPG2 was used to solve the CNOPs and FSV. In this paper, the CNOPs and FSV are numerically obtained by solving the minimum of eqs (9) and (11) using the SPG2 as well. The SPG2 is a non-monotone projected gradient algorithm for solving large-scale convex-constrained optimization problems (Birgin et al., 2001). It combines the classical projected gradient method with the spectral gradient choice of step length and a non-monotone line-search strategy. The user needs to define an objective function and provide the gradient values, and a constraint condition. In this research, the WRF adjoint model is used to compute the gradient of the cost function, the tangent linear model is employed to describe the linear evolution of a perturbation to obtain the FSV. Please refer to Xiao et al. (2008) and Huang et al. (2009) for details about the WRF tangent linear and adjoint models.

3. Experiment design

3.1. The model

The ARW model is used as the forecast model. The WRF is the next generation mesoscale model designed to serve both operational forecasting and atmospheric research applications. The model uses a third-order Runge–Kutta time integration, third- to fifth-order advection operators and split-explicit fast wave integration conserving both mass and energy. Like the total energy SVs (Majumdar et al., 2006) used as adaptive guidance for Atlantic tropical cyclone without moist physics, moist physics issues are not addressed in this study, that is, only the dry WRF model and its corresponding tangent linear and adjoint models with simple horizontal and vertical diffusion and surface drag are used. We will address the moist physics issues when more physics processes in the WRF tangent linear and adjoint models are developed.

3.2. Description of cases

Two cases are studied here. The first is the fast straight moving tropical cyclone Matsa (2005), which made landfall on 5 August in China. In this case, we are interested in the landfall prediction. The second case is a slow moving recurving tropical cyclone, Shanshan (2006). It began to recurve northwest after 1200 UTC 13 September. We focus on the sensitivity area during the recurving period.

Synoptic analyses indicate that Matsa developed from a tropical depression over the northwest Pacific Ocean on 30 July 2005. The depression continued to organize as it moved steadily westward, gradually intensified as it moved steadily northwestward and late on 1 August it strengthened into a tropical storm. Matsa approached the coast of China and made landfall late on 5 August in the southern region of Zhejiang Province, China. At 0000 UTC 6 August 2005, Matsa was southwest to the subtropical high and east to the middle level trough (Fig. 1a). The upper level trough and the south Asian high are to the west of Matsa (figure not shown).

The second case is a slow moving recurving tropical cyclone, Shanshan (2006). It developed from a tropical depression over the northwest Pacific Ocean and reached moderate typhoon intensity on 11 September. It moved westward and turned northwestward after 1200 UTC 13 September and finally made landfall in Japan. It is influenced by a separated subtropical high and a mid-level trough as shown in Fig. 1b. Compared to observation maximum wind speed at the time, NCEP analysis gives a weak tropical cyclone Shanshan.

3.3. Experiment setup

One domain with 60 km resolution was configured for all of the simulations. The domain had $151 \times 97 \times 15$ grid points using the Mercator projection centred at 120°E, 28°N, which is shown in Fig. 1. The model top is 50 hPa. The simulation period is 36 h for the two cases. For typhoon Matsa, the model is initiated at 1200 UTC 4 August 2005 to cover its landfall and Shanshan at 1200 UTC 13 September 2006 to cover its recurving period.

Two control runs are carried out to generate the basic state trajectories of typhoons Matsa and Shanshan. The initial conditions are interpolated from the NCEP $1^\circ \times 1^\circ$ final operational global analysis by the WRF pre-processing system (WPS). The NCEP data for this study are from the Research Data Archive (RDA), which is maintained by the Computational and Information Systems Laboratory (CISL) at the National Center for Atmospheric

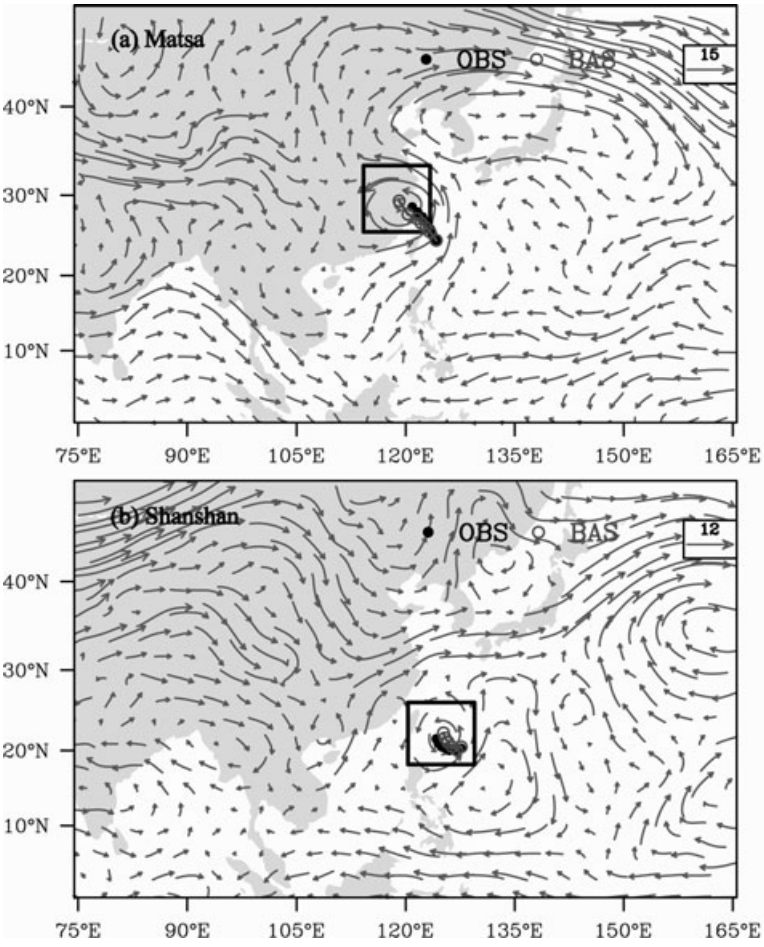

Fig. 1. The 36-h observed tracks and simulated tracks with overlay of background wind of typhoons: (a) Matsa and (b) Shanshan. For typhoons Matsa and Shanshan, the model is initiated at 1200 UTC 4 August 2005, and 1200 UTC 13 September 2006, respectively. The observed track (OBS) is shown by the curve with filled black dot and the simulated track (BAS) is presented by the curve with grey circle. The black rectangle presents the verification area. The wind vector at the model initialization time from GFS analysis is shown by grey vector.

Research (NCAR) (http://dss.ucar.edu/datasets/ds083.2/). The simulated typhoon tracks in the basic trajectories (hereafter named as BAS) and the observed tracks (hereafter named as OBS) are shown in Figs 1a and b. The model tracks agree well with the observation for the two cases. Figure 1a shows that the model produces a straight northwestward movement of Matsa and makes landing well. It also simulates the recurvature of Shanshan, but gives a slight northward track bias (Fig. 1b).

The CNOP and FSV are numerically obtained by the SPG2 algorithm with a 36-h optimization period. The initial conditions interpolated from the NCEP analysis in the control runs also provide the initial value of $\mathbf{x_0}$ in eqs (9) and (11) to obtain CNOP and FSV. The verification region is chosen to cover the whole forecasted tropical cyclone at 36 h. The verification regions of Matsa and Shanshan are shown by the rectangle in Figs 1a and b, respectively. The local projection operation P is 1(0) inside (outside) the verification region. The β is chosen to make it the corresponding maximum wind component of about 6 m s^{-1} and the maximum temperature amplitude of 2 K at the initial time, which is reasonable value of analysis increment in the current WRF-4DVAR data assimilation system. The background error statistics matrix **B** is adopted from a WRF-3DVAR system running in the Central Weather Bureau in Taiwan (Hsiao et. al., 2010). The **B** is calculated by the National Meteorological Center (NMC) method (Parrish and Derber, 1992). The **B** is formulated in control variable space. The control variables here are streamfunction, the unbalanced components of velocity potential, temperature and surface pressure and 'pseudo' relative humidity. The 'unbalanced' control variables are defined as the difference between full and 'balanced' (or correlated) components of the field with the streamfunction (Barker et al., 2004). An additional description of the background error matrix **B** can be found in Hsiao et al. (2010).

4. Comparison of CNOPs and FSVs

The patterns of CNOP and FSV at the initial time are compared in this section. The results show a local CNOP in both tropical cyclone cases. As will be shown in Section 5, the total energy of the local CNOP at the end of the final time is larger than the FSVs. It may play an important role in targeting, thus the local CNOP is also illustrated. We find that the wind components of the initial and evolved perturbations are larger than the temperature perturbations and the initial humidity perturbation is nearly zero. One reason is that the adiabatic model was employed. In the remainder of this paper, only the wind component perturbations are shown.

4.1. Horizontal structures

For the Matsa case, Figs 2–4 illustrate the horizontal structures of CNOP, FSV and local CNOP at a low level ($\eta = 0.805$, approximately 825 hPa), middle level ($\eta = 0.4115$, approximately

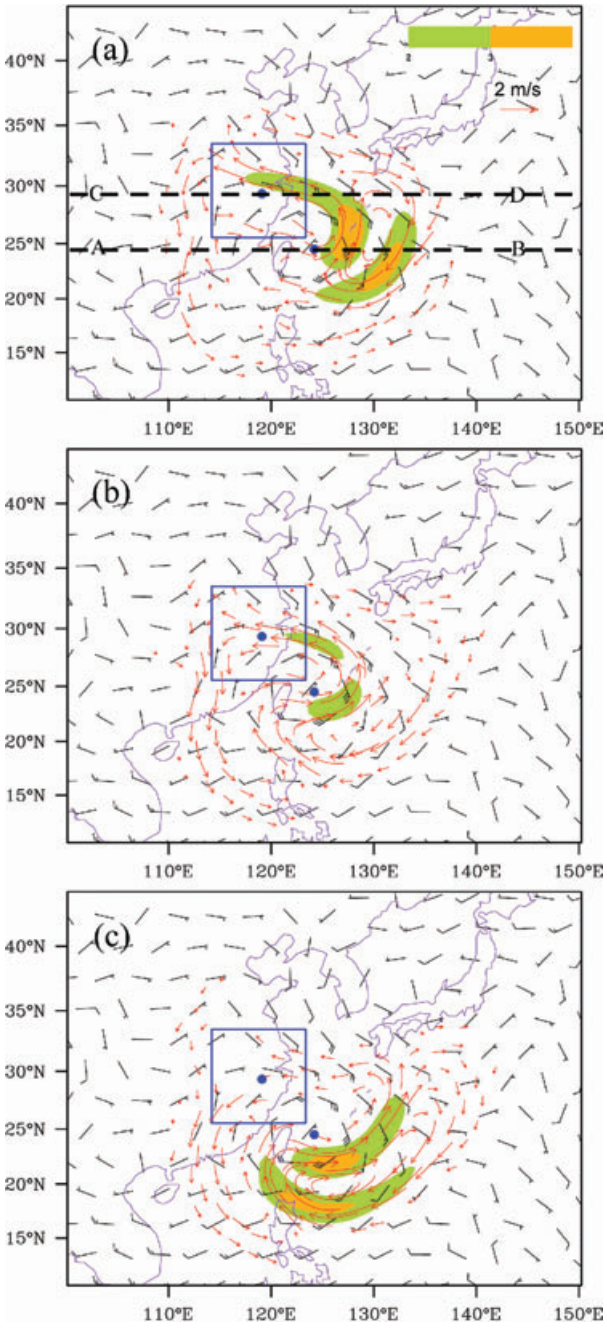

Fig. 2. The Matsa case. Wind (stream) and its speed (shaded; m s^{-1}) of perturbations at η level 0.805 (about 825 hPa). (a) CNOP, (b) FSV and (c) Local CNOP. Background wind (barb) is also shown; a full barb is 10 m s^{-1}. The blue boxes indicate the verification region. The two circles indicate the initial and final position of the tropical cyclone. The vertical section of perturbations will be shown along the black dash lines AB and CD in (a).

470 hPa) and upper level ($\eta = 0.119$, approximately 200 hPa) of the troposphere. The structure of the initial CNOP is different from that of the FSV although both are localized and have clear patterns. In the lower troposphere (Fig. 2), the maximum wind

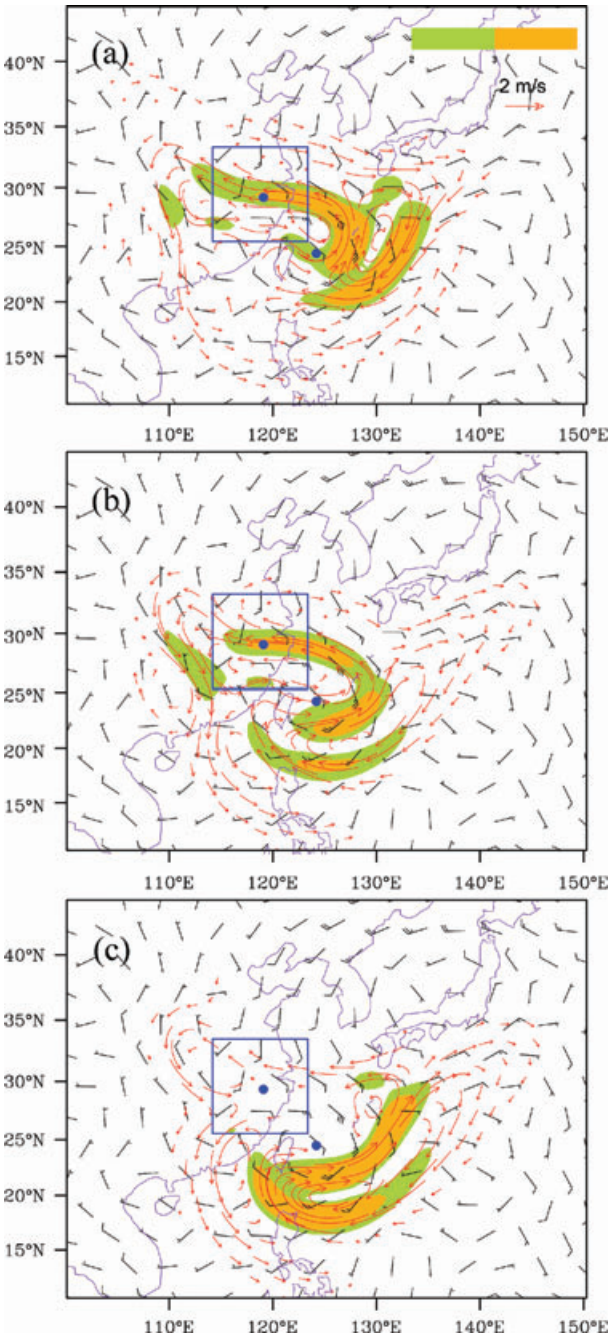

Fig. 3. As in Fig. 2, but at η level 0.4115 (approximately 470 hPa). (a) CNOP, (b) FSV and (c) Local CNOP.

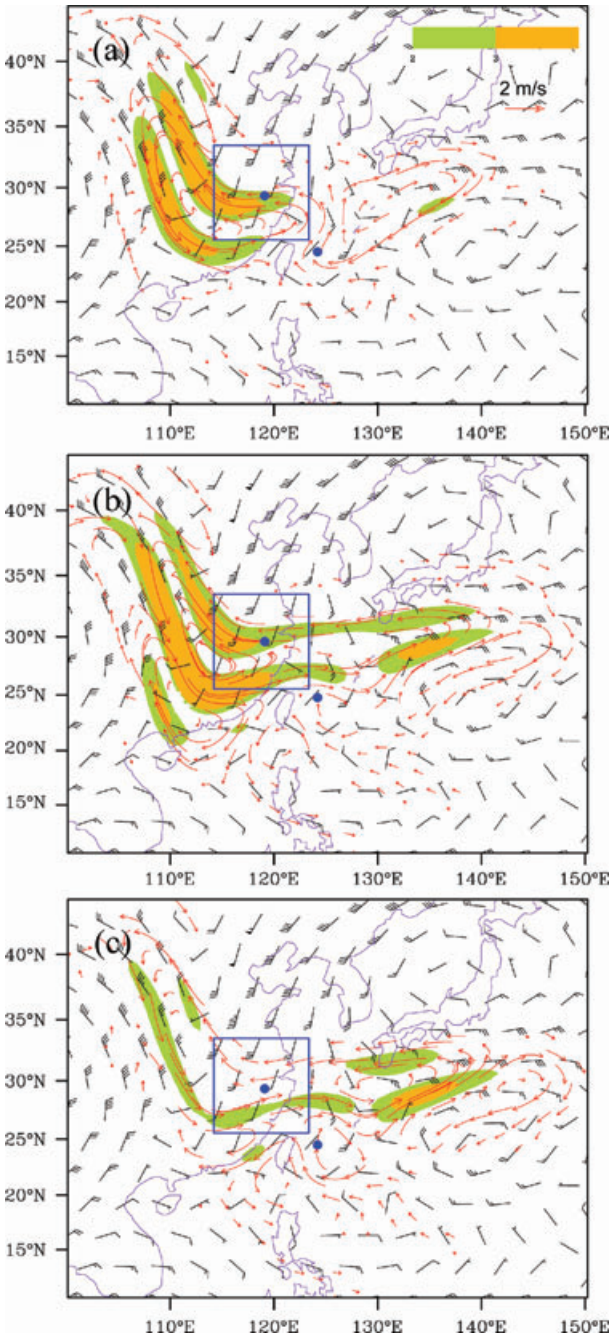

Fig. 4. As in Fig. 2, but at η level 0.119 (approximately 200 hPa). (a) CNOP, (b) FSV and (c) Local CNOP.

speed is near the region of large background wind speed on the east of the tropical cyclone centre for all perturbations and both the CNOP and the FSV have a quasi-dipole structure. It can see that the speed of CNOP and local CNOP is larger than FSV. In addition, the location of the maximum wind speed centre is very different among various perturbations. For the CNOP, the maximum wind speed is on the east and northeast of the typhoon centre, but for the FSV, it is located on the southeast of the typhoon centre. For the local CNOP, the maximum wind speed is located in the southeast quadrant.

In the mid-troposphere (Fig. 3), both the CNOP and the FSV show two regions with large wind speeds. One is an area of maximum wind speed ahead of the trough over continental China and the other is near the typhoon centre. The maximum perturbation

wind speed is somewhat near the region of large background wind speed on the east of the tropical cyclone centre. The maximum speed near the typhoon from the CNOP is smaller than from the FSV. For the local CNOP, the maximum is located near the typhoon centre. In the upper level (Fig. 4), the areas of large sensitivity are associated with the trough ahead the south Asian high for the CNOP and the FSV. There are still some signals near the southwest of the subtropical high for the local CNOP. It is found that the perturbations are located in the region of large wind speed in the background (e.g. Fig. 3, wind larger than 10 m s^{-1} shown by two or more barbs).

The Matsa case was also investigated in MZW2009, it was found that for the CNOP the maximum values of wind were located at the northeast side of the cyclone centre. However, in this research, it is found that for the CNOP, the maximum wind speed is on the east and northeast of the typhoon centre, for the local CNOP, the maximum wind speed is located in the southeast quadrant. A reason for the difference is that the optimization time is 36 h in this study, which is 12 h longer than the one in MZW2009. With the 36-h optimization time, the perturbation in the upstream of the northeast side of cyclone centre can have an impact on the verification region.

For the Shanshan case, Figs 5 and 6 show the horizontal structures of the CNOP, FSV and the local CNOP at the lower level ($\eta = 0.805$, approximately 825 hPa) and middle level ($\eta = 0.4115$, approximately 470 hPa) of the troposphere. The perturbations in the upper level are not shown since they do not have clear structures and have small wind speeds. The CNOP, local CNOP and FSV are localized and have clear spatial structures in the lower and middle troposphere. In the lower troposphere (Fig. 5), the maximum wind speed of the CNOP and the local CNOP is larger than the FSV. The maximum perturbation is located to the south and northwest of the typhoon centre for the CNOP, the east and northwest for the local CNOP and the south and north for the FSV. Both the CNOP and the FSV have a quasi-dipole structure. In the mid-troposphere (Fig. 6), the CNOP, local CNOP and the FSV possess similar wind speed amplitudes. The maximum perturbation is to the southwest of the typhoon centre for the CNOP, north for the local CNOP and southwest for the FSV. There are no significant signals found in the upper troposphere.

For the Shanshan case, the sensitivity region is near the typhoon centre at the time. This feature is consistent with the results in Wu's research (Wu et al., 2009b) by use of ADSSV method. In his research, it was found that at 0000 UTC 14 September, which is 12 h later than this paper, the ADSSV showed that the major sensitive regions were located around typhoon Shanshan, with the maximum sensitivity to the southeast of the centre and the local maxima to the northwest. There is no sign of ADSSV features associated with the mid-latitude trough around the time. However, at 0000 UTC 15 September and after the time, two major ADSSV features were identified. One was located at about 800 km to the southeast of Shanshan and the other occurred in the mid-latitude trough region at 500 hPa near northern-central China.

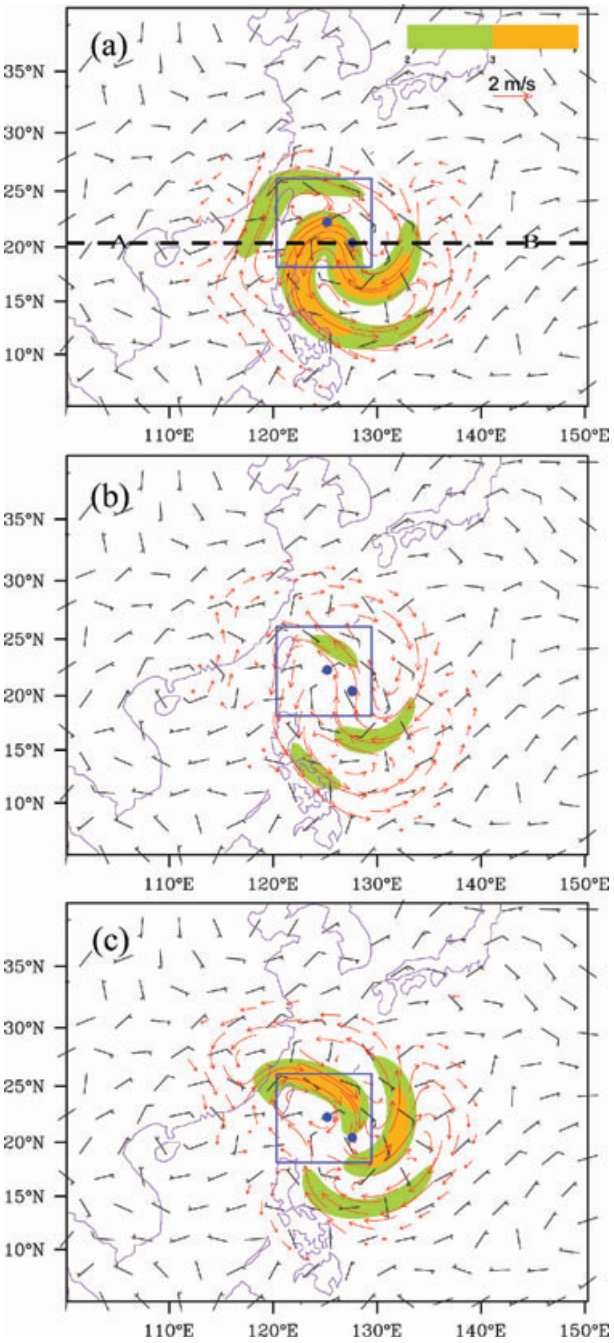

Fig. 5. As in Fig. 2, but for the Shanshan case and at η level 0.805 (825 hPa). (a) CNOP, (b) FSV and (c) Local CNOP.

Since the wind components of the initial and evolved perturbations are larger than the temperature perturbations, we examined the spatial distribution of perturbations using a kinetic energy tendency equation to determine the causes. In a pressure coordinate, a horizontal kinetic energy tendency equation neglecting

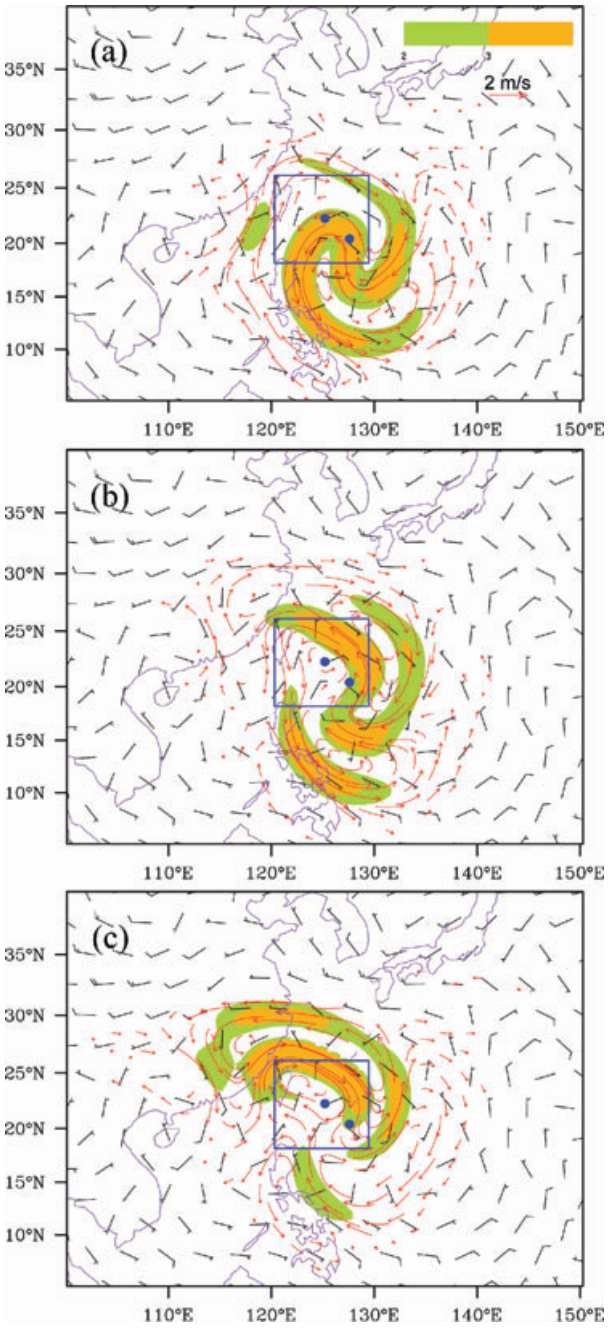

Fig. 6. Same as Fig. 2, but for the Shanshan case. (a) CNOP, (b) FSV and (c) Local CNOP at η level 0.4115 (470 hPa).

moisture and diffusion effects, may be written as

$$\frac{DK}{Dt} = -\mathbf{V} \cdot \nabla \Phi, \tag{12}$$

where $\nabla = (\partial_x, \partial_y)$ is the horizontal gradient, $D/Dt = \partial_t + \mathbf{V} \cdot \nabla + \omega \partial_p$ is the material derivative, K is the kinetic energy of the horizontal wind, $\mathbf{V}$ is the horizontal wind vector, ω is the vertical velocity and Φ is the geopotential height. It is seen from eq. (12) that the energy tendency $\frac{DK}{Dt}$ depends on the geopotential height gradient forcing term, $-\mathbf{V} \cdot \nabla \Phi$. Given a perturbation wind vector $\delta\mathbf{V}$, if $\delta\mathbf{V}$ is parallel to $-\nabla\Phi$, it will obtain energy from background or transport energy into background, and the larger absolute value of $-\nabla\Phi$, the larger charge of $\frac{DK}{Dt}$. For the local energy change of $\partial_t K$, in addition to the geopotential height gradient forcing, it also depends on $\mathbf{V} \cdot \nabla K$, the background wind speed and energy gradient. If a perturbation wind vector $\delta\mathbf{V}$ is parallel to ∇K, the larger absolute value of ∇K, the larger charge of $\partial_t K$. If $\delta\mathbf{V}$ is parallel to $\mathbf{V}$, it can result in increasing or decreasing $\mathbf{V} \cdot \nabla K$ as well. So that we can see that the $\delta\mathbf{V}$ distribution should be somewhat be controlled by the distribution of $-\nabla\Phi$, $\mathbf{V}$ and ∇K.

Figures 7a–f depict the distributions of $||-\nabla\Phi||$, $||\mathbf{V}||$ and $||\nabla K||$ of the Matsa case and Shanshan case, respectively. Here, $||\mathbf{x}||$ is defined as the square root of the inner product of variable $\mathbf{x}$ and itself. By comparing Fig. 3 to Figs 7a–c, and Fig. 5 to Figs 7d–f, it is seen that the larger signal of the CNOP, FSV and local CNOP are located in or near the region of larger geopotentail gradient, wind speed and the large gradient of background energy. This indicates that the distributions of perturbations are somewhat controlled by the distribution of background goepotential and wind.

Given a perturbation wind vector $\delta\mathbf{V}$ with perturbation energy δK, the difference between CNOP and FSV is that the nonlinear term $\delta\mathbf{V} \cdot \nabla \delta K$ is not considered during the optimization. However, the CNOP and local CNOP can result in larger nonlinear terms than those induced in the FSV (Fig. 8). So the nonlinear term is an important factor resulting in the distribution of perturbations. The non-linear terms of CNOP and local CNOP are significantly larger than those of FSV during the evolution of perturbations (figures not shown). This also supports the view that CNOP may be more important in tropical cyclone prediction as noted in MZW2009.

To summarize, two regions of sensitivity with larger wind speeds are found in the initial perturbations of the Matsa case. One is near the typhoon centre and is associated with the subtropical high, whereas the other is over east China and is associated with mid-latitude trough. This indicates both the subtropical high and the mid-latitude trough will have a significant influence on the tropical cyclone's evolution. Certain tropical cyclone cases with two sensitive regions have also been found by other researchers (e.g. Wu et al., 2009a). For Shanshan, the sensitivity region is near the typhoon centre. In both cases, the details in the pattern and the distribution of the maximum wind speed are different among the various perturbations. The CNOP and local CNOP have stronger wind speeds than that of FSV at low to mid-level of troposphere, whereas the FSV has larger signals in the upper level, as will be shown in the vertical structures in the Subsection 4.2. The distribution of perturbations can partially be related to the distribution of maximum background geopotential height gradient, wind speed and wind energy gradient. The nonlinear term $\delta\mathbf{V} \cdot \nabla \delta K$ is also an important factor resulting in the distribution of perturbations.

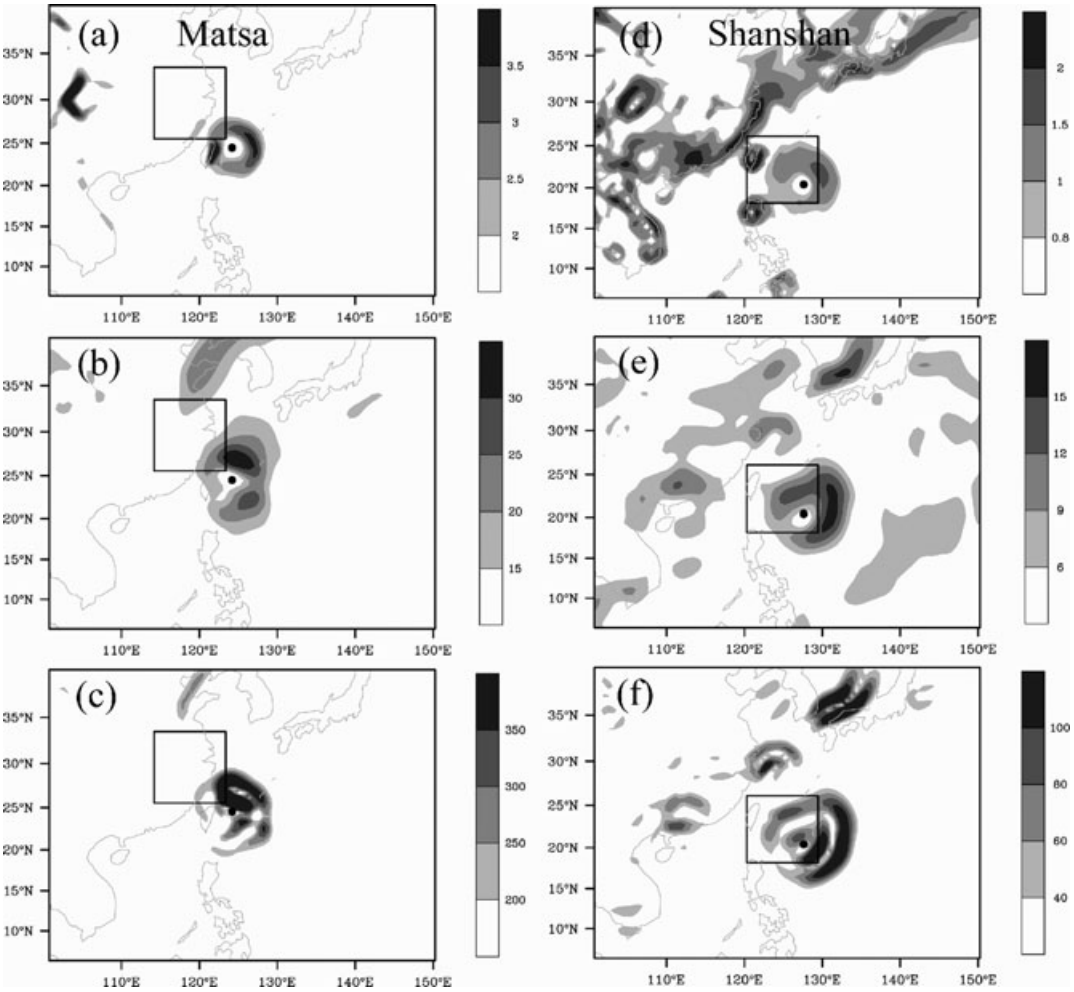

Fig. 7. The distribution of (a) and (d) $||-\nabla\Phi||$, (b) and (e) $||\mathbf{V}||$ and (c) and (f) $||\nabla K||$ of the Matsa at η level 0.4115 (left-hand panels) and Shanshan case at η level 0.805 (right-hand panels), respectively. $||\mathbf{x}||$ is defined as the square root of $\langle \mathbf{x}, \mathbf{x} \rangle$.

4.2. Vertical structures

The two regions of sensitivity found in the mid-troposphere in the Matsa case are also shown well in the vertical west–east cross-sections of perturbation wind (Fig. 9). Two cross-sections along the lines AB and CD in Fig. 2a are plotted. The lines AB and CD are chosen to cross the tropical cyclone centre at initial time and final time, respectively. In the perturbations to the east of the typhoon centre, the CNOP and the local CNOP have a quasi-barotropic structure, but for the FSV, it has a moderately eastward tilt. For the perturbations near the mid-level trough (Figs 9b, d and f), the CNOP has a considerable westward tilt, whereas the FSV and the local CNOP only have a slight tilt. It is also seen that the larger wind perturbations of the CNOP and the local CNOP near the typhoon centre are located in the mid and low troposphere, but for the FSV, it is mainly located above the mid-troposphere.

The west–east cross-sections of Shanshan are shown in Fig. 10. The perturbation wind (shaded) and background v wind (contour) of the CNOP, FSV and the local CNOP along lines the AB in Fig. 5a are presented. It is seen that the maximum wind speed is mainly located in the middle and lower levels of the troposphere. The perturbations have a quasi-barotropic structure. Eastward tilts are found in the CNOP and the FSV in the upper troposphere. For the FSV and the local CNOP, the perturbations are mainly to the east of the typhoon centre. The perturbations are on both sides of the typhoon centre in the CNOP. For the two cases, we also look at the cross-sections along other lines and get the similar conclusion.

In summary, the perturbations in the two cases studied earlier are generally near the typhoon. In the Matsa case, an additional large perturbation that is close to the mid-level trough is also found. Compared with FSV, CNOP and local CNOP have larger wind speed at low to mid-level troposphere. The CNOP and local CNOP are nearly quasi-barotropic around the typhoon, but the FSV has an easterly tilt. All the perturbations have a westerly tilt near the mid-level trough in the Matsa.

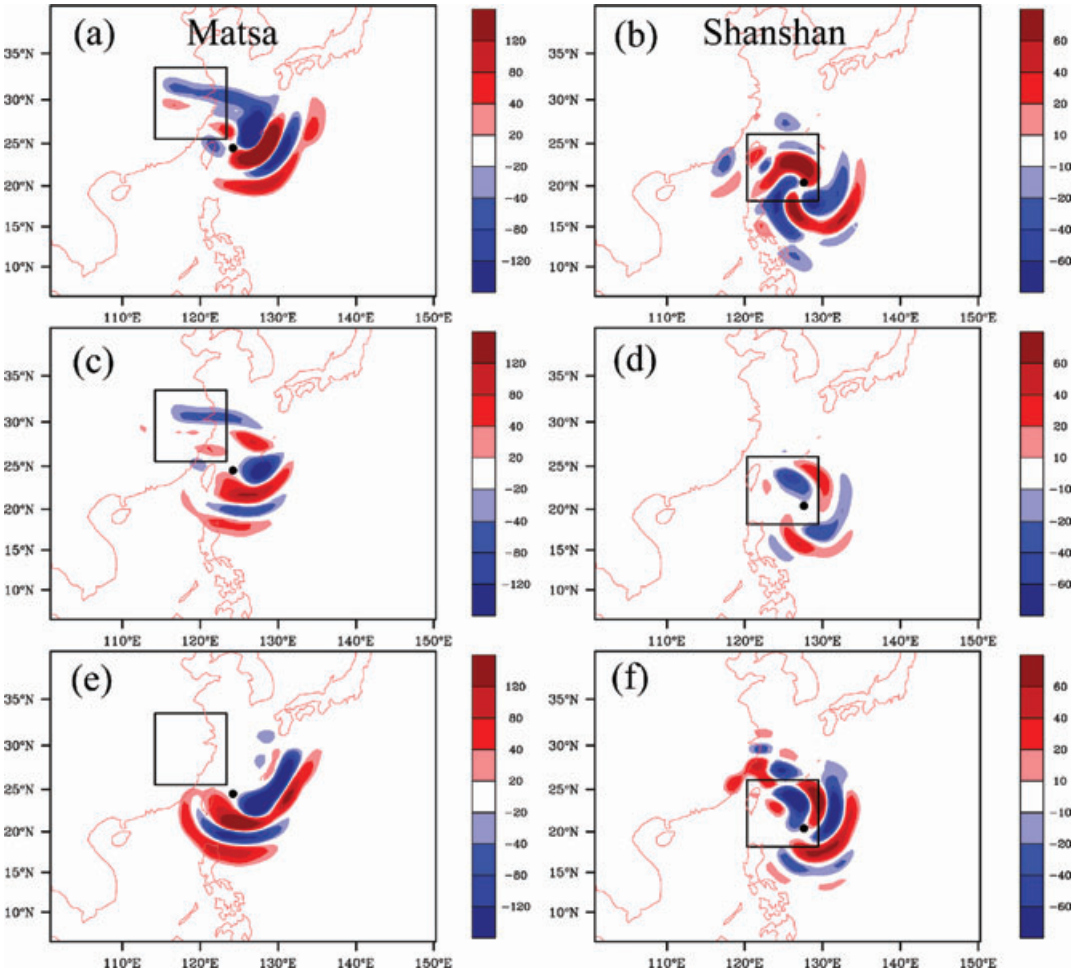

Fig. 8. The distribution of the non-linear term $\delta\mathbf{V} \cdot \nabla\delta K$. (a) and (b) CNOP, (c) and (d) FSV and (e) and (f) Local CNOP of the Matsa at η level 0.4115 (left-hand panels) and Shanshan case at η level 0.805 (right-hand panels), respectively.

5. The evolution of CNOPs and FSVs

5.1. Structures

The non-linear evolution of a perturbation $\boldsymbol{\delta x_0}$ is obtained by computing the difference of two WRF runs with the initial conditions $\mathbf{x_0} + \boldsymbol{\delta x_0}$ and $\mathbf{x_0}$, respectively. The result of the Matsa case is addressed first. Figs 11 and 12 compare the non-linear evolution of perturbations at the end of the optimization time at the middle and upper levels. As seen in Figs 11 and 12, the CNOP, FSV and the local CNOP evolve into the verification area at 36 h with structures possessing a quasi-dipole pattern. The wind directions through the quasi-dipole among the developed perturbations are different. The wind direction is northward in the developed CNOP, mainly eastward in the local CNOP and northeast for FSV. In addition, the development of wind of CNOP and local CNOP is larger than that of the FSV at the low to mid-troposphere. However, the FSV has stronger development at the upper level (figure not shown).

For the case of Shanshan, the non-linear evolution of perturbations at the end of the optimization time at the low and middle levels are shown in Figs 13 and 14. After 36 h of development, the CNOP, the FSV and the local CNOP evolve into structures possessing a quasi-dipole pattern. The wind directions in the quasi-dipole are also different. The wind direction is westward in the developed CNOP, mainly southeast in the local CNOP and northward for the FSV. Similar to the Matsa case, the maximum wind speed of the CNOP and the local CNOP are larger than the FSV in the low to mid-troposphere.

It seems that the spatial scale becomes larger when the perturbation evolves. We perform a spectral analysis on the wind perturbation fields using the method developed by Errico (1985). Figures 15a and b depicts the spectra of the u component perturbations in the Matsa case at the start and the end of the optimization period, respectively. At the start of the optimization period, the CNOP shows a bit larger variance than the FSV in the smaller scale range (where the wavelength is shorter than

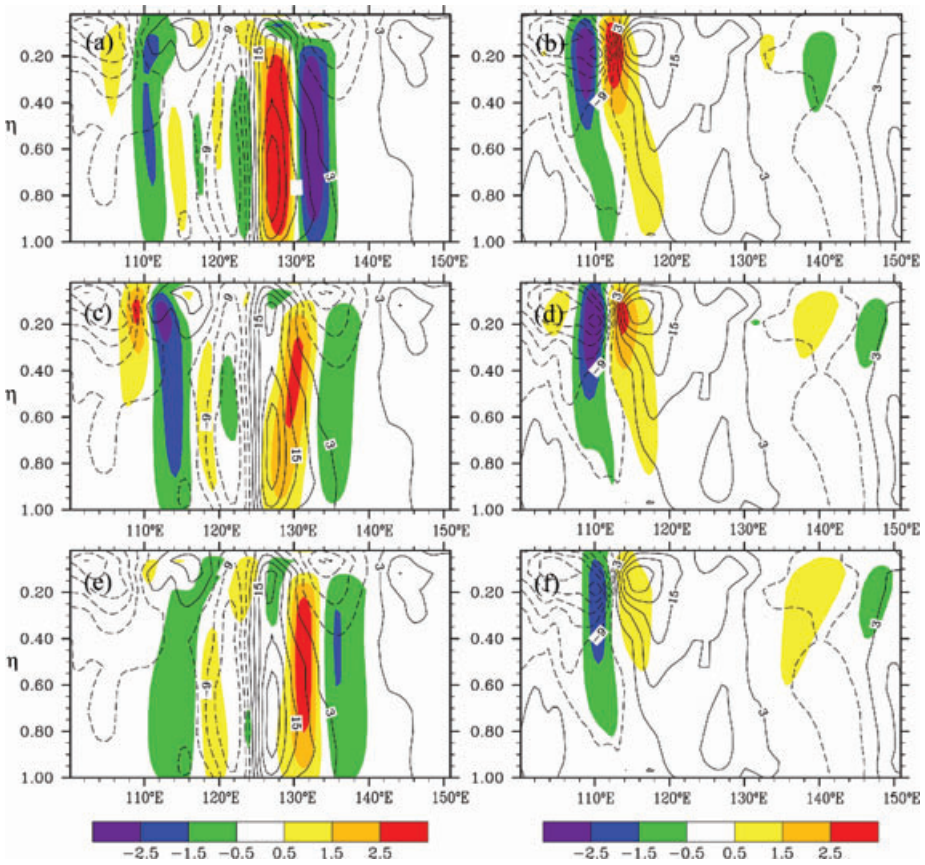

Fig. 9. The Matsa case. The west–east cross-sections of perturbation wind (shaded) and background wind (contour) for (a) and (b) CNOP, (c) and (d) FSV and (e) and (f) local CNOP along lines AB at 24.5°N (left-hand panels) and CD at 29.4°N (right-hand panels) in Fig. 2a.

1500 km), but nearly the same in the large-scale range. At the start time, the u component of the CNOP, local CNOP and the FSV are mainly concentrated in the smaller scale range roughly from 800 to 1500 km. At the final time, the maximum variance is located in the large-scale range. The spectra show the upscale growth of various perturbations during the optimization period. The spectra of the v perturbations show an upscale growth as well; therefore, the figures are not shown. Similar upscale growth of various perturbations during the optimization time period is also found in the Shanshan case (figures not shown). At the starting time, the u component of the CNOP is mainly concentrated at the scale of about 1400 km, whereas the local CNOP and the FSV are mainly concentrated in the smaller scale range at about 800 to 1500 km. At the final time, the maximum variance is located in the scale range larger than 1500 km.

5.2. *The evolution of total energy*

The above results from the two cases illustrate that the perturbations reach the verification area after 36 h of development. The CNOP and local CNOP have the largest impact on the forecast in the verification area. This is clearly shown in the total energy at the final time. Figure 16 compares the total energy evolution of the CNOPs and the FSVs in the verification region during the optimization time period. It is obvious that Matsa's CNOP development is larger than the others, whereas the local CNOP little smaller over the last 6 h, and the energy of the FSV develops the least of all. At the final time, the energy of the CNOP is about two times that of the FSV. The CNOP has the largest impact during the whole forecast, whereas the local CNOP has the smallest impact over the first 24 h and develops rapidly over the last 12 h. For Shanshan, the evolution of the perturbations has a similar growth rate over the first 18 h. However, the CNOP and the local CNOP develop faster over the last 18 h, reaching their maximum at the final time. The energy of the CNOP is about 1.5 times that of the FSV at the final time.

5.3. *The impact on track simulation*

In this section, we will examine the impact of perturbations on tropical cyclone track simulation. As we mentioned in the Introduction, the norm plays an important role in the computation of the CNOP and the FSV. It should be chosen according to the problems studied. The total energy norm has been used in

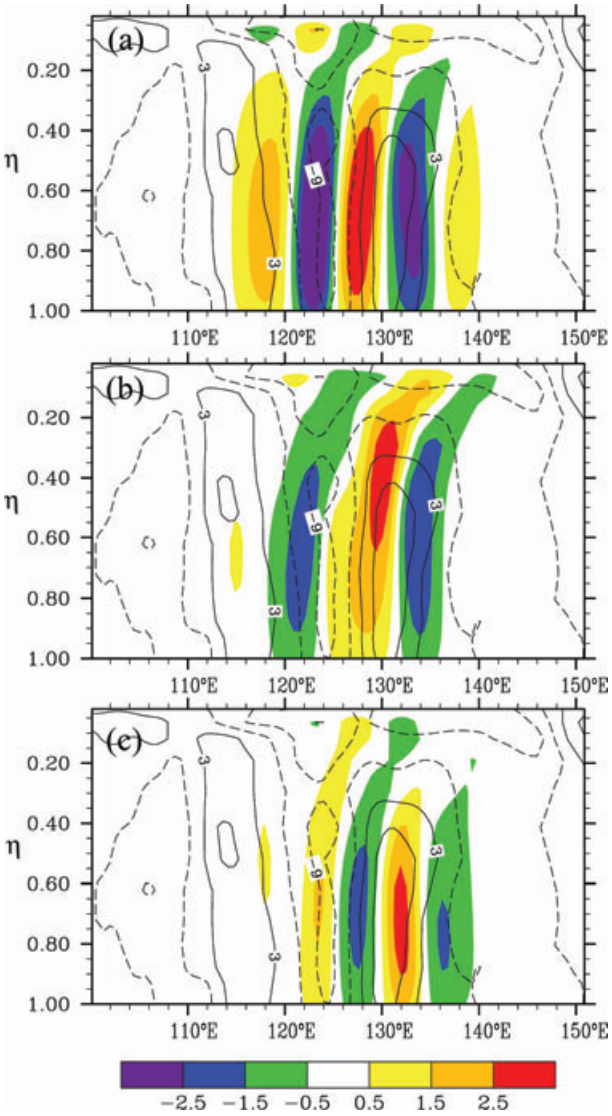

Fig. 10. The Shanshan case. The west–east cross-sections of perturbation wind (shaded) and background wind (contour) for (a) CNOP, (b) FSV and (c) Local CNOP along lines AB at 20.4°N in Fig. 5a.

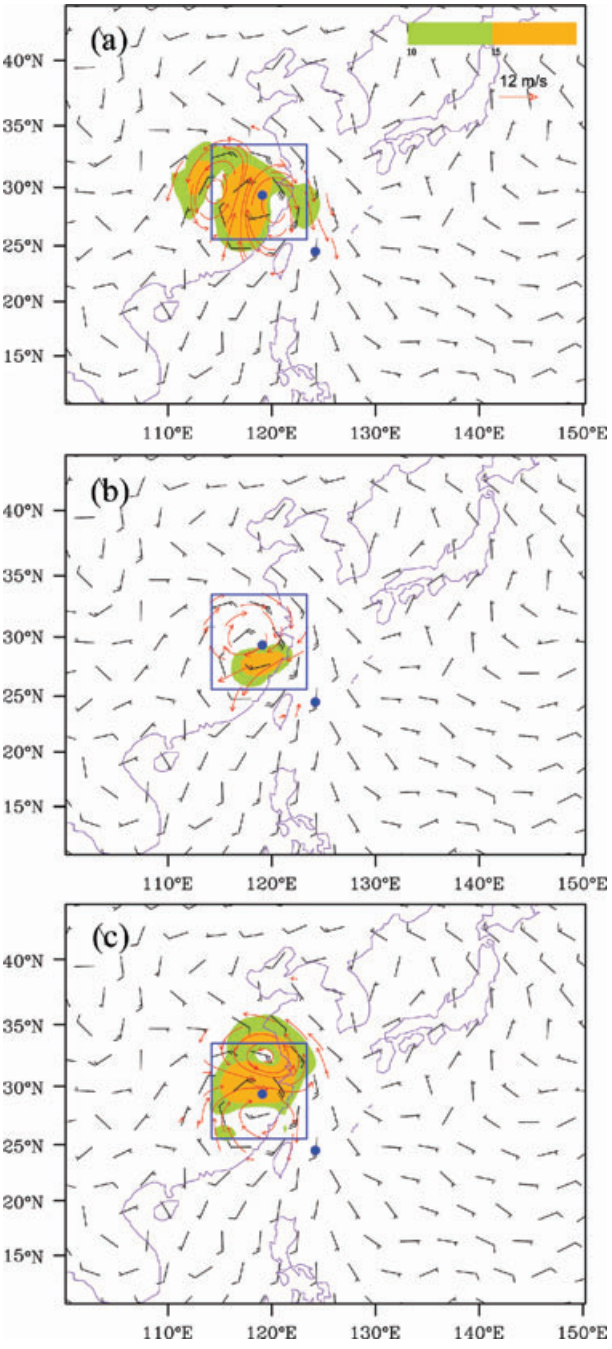

Fig. 11. The Matsa case. The evolved perturbations of (a) CNOP, (b) FSV and (c) Local CNOP at η level 0.805 (825 hPa).

previous research by Mu et al. (2007, 2009). Since the total energy norm is not directly related to the typhoon movement, we wonder whether the perturbation with the largest energy development at the final time will have the greatest impact on typhoon track simulations in terms of track distance error. At least, its impact is comparable to the FSV. If that is true, we expect that the total energy norm at the final time would be helpful in targeting to improve the track forecast skill.

The impact of the CNOPs and FSVs on tropical cyclone track simulation is investigated, and the simulated typhoon tracks are plotted in Fig. 17. It is clear that for the Matsa all the perturbations have a greater impact on the simulated tracks in terms of track distance from the BAS at the final time; however, the CNOP has the largest impact among the perturbations at the final time. The CNOP and local CNOP drive the Matsa to move faster than the BAS, whereas the FSV slows the movement of the Matsa. For the Shanshan, all the perturbations have a similar impact on track simulation in terms of track distance from the BAS at the final time. However, when looking at their impacts on the

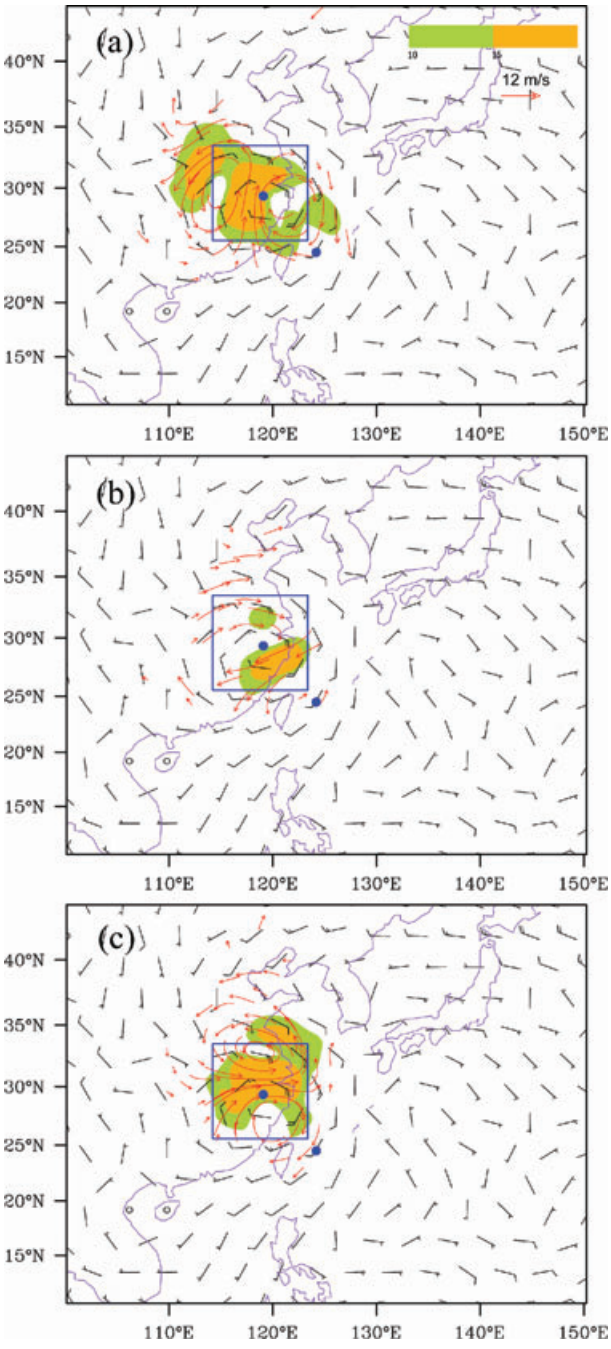

Fig. 12. The Matsa case. Non-linear evolutions of (a) CNOP, (b) FSV and (c) Local CNOP at η level 0.4115 (470 hPa).

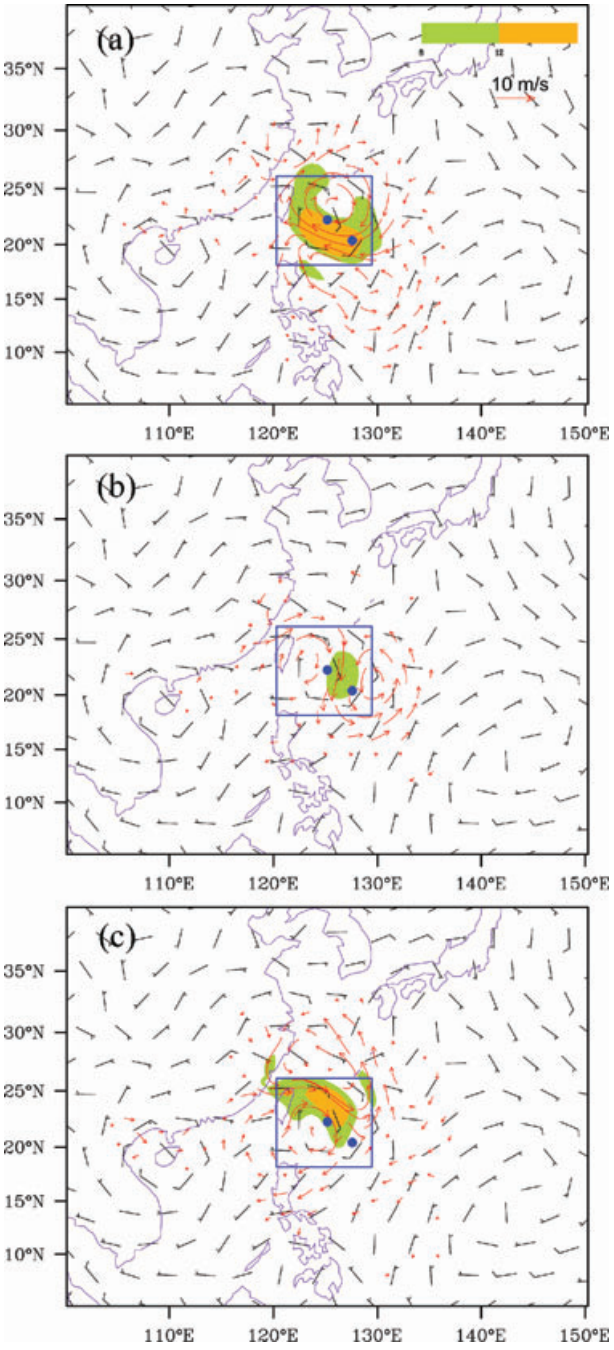

Fig. 13. The Shanshan case. Non-linear evolutions of (a) CNOP, (b) FSV and (c) Local CNOP at η level 0.805 (825 hPa).

movement direction of tropical cyclone, the difference between CNOP and FSV is significant. The CNOP drives the Shanshan to move westward, whereas the FSV drives the Shanshan to move northward. The local CNOP drives the Shanshan to move northward faster than FSV. Note that the CNOPs cause large prediction spread, which means it may be helpful in generating members for ensemble forecast (Jiang and Mu, 2009).

Though the total energy norm at the final time is not directly related to typhoon movement, we find that CNOPs have a larger, or at least a similar impact on the tropical cyclone track simulation compared to the FSVs in terms of track distance from the BAS. This is an indication that even when focusing on track forecast, the CNOP with norm of background error at the

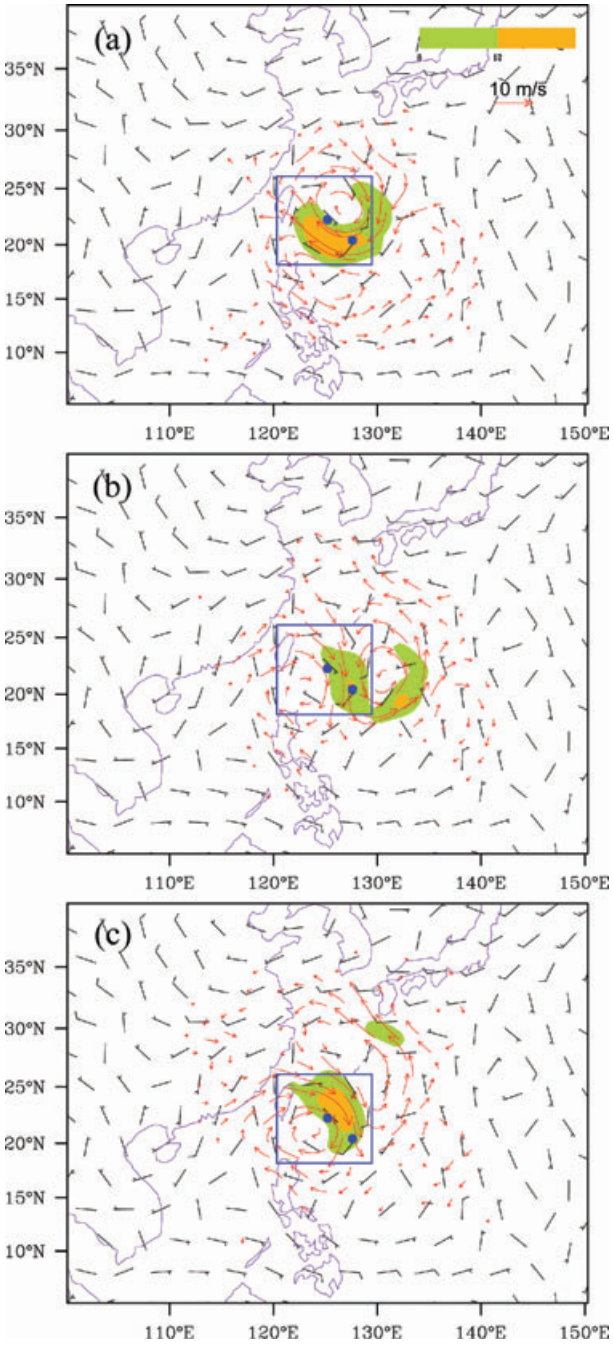

Fig. 14. The Shanshan case. Non-linear evolutions of (a) CNOP, (b) FSV and (c) Local CNOP at η level 0.4115 (470 hPa).

initial time and total energy norm at the final time is a reasonable candidate for tropical cyclone targeting.

6. Summary and discussions

The potential application of the CNOP method to tropical cyclone adaptive observation was studied in the frame of the WRF-4DVAR system. The WRF-4DVAR system provides advanced dynamics and a realistic background error estimation model. The background error norm is a reasonable choice since the CNOPs are expected to reveal the rapid growth of error in the background. Hence, we expect that additional observations in the region identified by the CNOPs will reduce the initial condition error efficiently. Another benefit is that the same WRF model and background error statistics can be used in the targeting method, data assimilation and forecasting cycling systems. This will avoid mismatch among the targeting method, the data assimilation system and the forecast model, which is one of the causes of targeted observations having only neutral or even negative impact on forecasts (Langland, 2005).

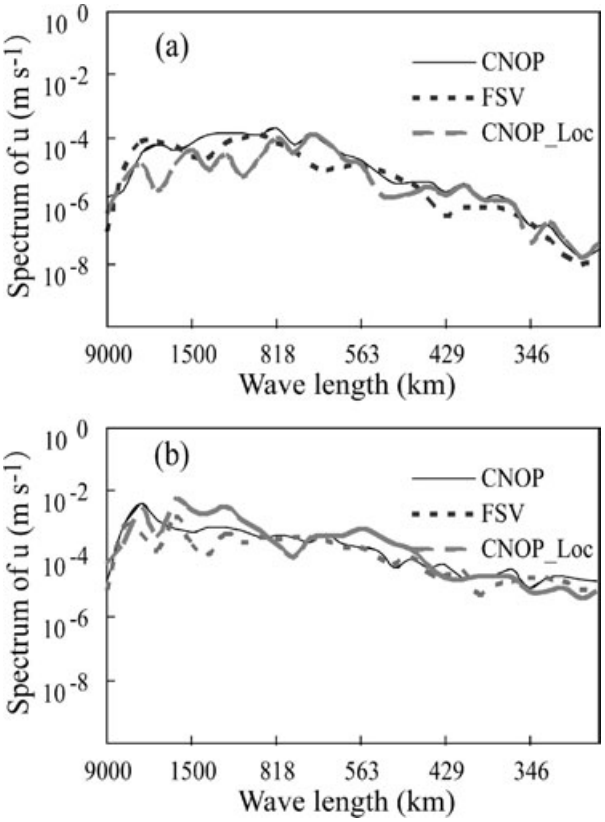

Fig. 15. The Matsa case. The spectra of u component at (a) initial time and (b) final time.

Both CNOPs and FSVs were numerically obtained by the SPG2 algorithm with a 36-h optimization time interval. The background error matrix was used as the constraint norm at initial time and the total dry energy metric was employed at final time. Two cases, a fast straight moving typhoon Matsa (2005) and a slow moving recurving typhoon Shanshan (2006) were studied. The spatial structures, their energies and their non-linear evolution of the CNOPs during the optimization time period were compared with those of the FSVs. The impact of the CNOPs and the FSVs on simulated tropical cyclone tracks was also discussed.

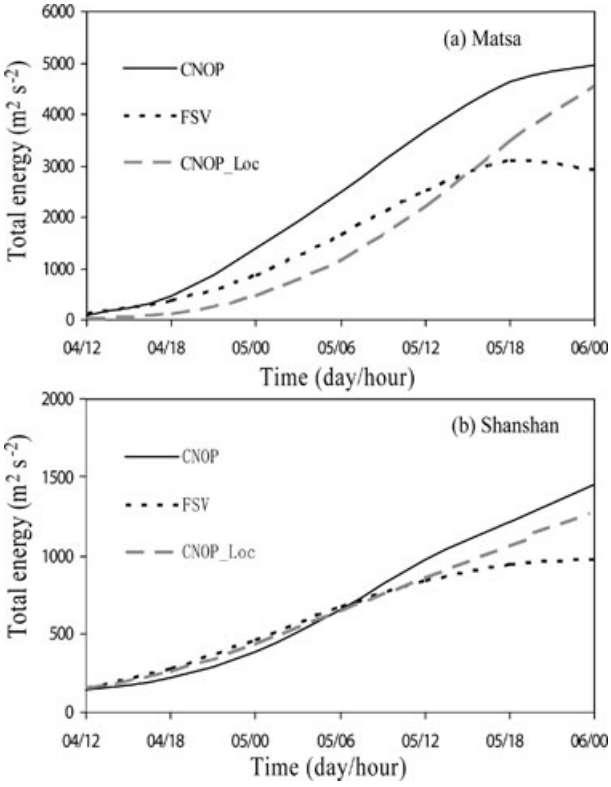

Fig. 16. The total energy development of CNOP, FSV and local CNOP during the optimization time period: (a) Mastsa and (b) Shanshan.

The results showed that the CNOP and FSV methods indicated similar large-scale sensitivity region distributions in the two cases. Two regions of sensitivity with larger wind speeds were found in the initial perturbations of the Matsa case. One was near the typhoon centre and was associated with the subtropical high, whereas the other was over east China and was associated with mid-latitude trough. It indicated both the subtropical high and the mid-latitude trough could have a major influence on the tropical cyclone evolution. Some tropical cyclones contained two sensitive regions were also found by other researchers (e.g. Wu et al., 2009a). For the Shanshan case, the sensitivity region was near the typhoon centre at the time. Both the CNOPs and the FSVs were localized and had quasi-dipole structures and evolved into the verification area at the final time with the upscale growth of perturbations in the two cases.

However, the detailed structure of CNOPs differed significantly from the FSVs in the each case in terms of the spatial pattern and the distribution of maximum wind speed. Compared with the FSV, in addition to the difference in the horizontal distribution of wind, the CNOP and the local CNOP had larger wind speed at low to mid-level troposphere, indicating the wind under mid-level troposphere was more important than the upper level wind. These differences could have an impact on the final decision of specific locations where the additional observations should be employed.

The growth rate of total energy and the impact on the track simulation of the CNOPs differed greatly from the FSVs. For the two cases, the total energy of the CNOP was about two times of that of the FSV at the final time. The CNOP (local CNOP) had the largest (larger) impact on forecast in the verification area at the final time compared with the FSVs, suggesting both the CNOP and local CNOP should be considered in tropical cyclone targeting. Though the total energy norm at the final time was not directly related to typhoon movement, we found that the CNOPs had larger, at least similar impact on tropical cyclone track simulation compared to the FSVs. This indicated that, the CNOP method with the norm of background error at the initial time and the total energy norm at the final time was a reasonable candidate in tropical cyclone targeting even for track prediction.

However, when focusing on tropical cyclone track prediction, the norms that are more directly related to typhoon movement are of interest. The DLM or 850–200 hPa average wind speed can be chosen because tropical cyclones are generally steered by the environmental DLM flow. By defining the steering flow of the tropical cyclone as an average of the environmental flow in the vicinity of the tropical cyclone centre, the tropical cyclone track simulation are more sensitive to initial perturbations in a barotropic model (Hoover and Morgan, 2010). As the fact that SVs are sensitive to the norm (e.g. Ehrendorfer and Errico, 1995; Ehrendorfer et al., 1999; Reynolds et al., 2007 and others), it is also of interest to compare the difference of the CNOP from the FSV with the energy norm or background error norm at initial time, and to examine how sensitive the CNOP is to the norms. The CNOP's sensitivity to verification specification is of interest as well (Zhou and Mu, 2011).

The reasons resulting in the spatial distribution of perturbations are examined by a kinetic energy tendency equation. It was found that the distribution of perturbations could partially be explained by the distribution of maximum background geopotential height gradient, wind speed and wind energy gradient. The non-linear term $\delta\mathbf{V} \cdot \nabla\delta K$ is also an important factor resulting in the distribution of perturbations. However, a detailed study of the properties of the CNOP and the reasons leading to the differences from the FSV are beyond the scope of this paper and will be the topic of future work. It is also worthwhile to investigate the properties of the CNOP in a moist model configuration when more physics processes in the WRF tangent linear and adjoint models are developed. Currently, we are working on the physics processes, such as microphysics, boundary layer parametrizations in the tangent linear and adjoint models of WRF. AKessler warm-rain scheme has been added into WRF tangent- linear and adjoint models, and has been applied into radar reflectivity assimilation (Wang et al., 2011). We also expect to perform more observation impact diagnostic studies to evaluate the impact of the CNOP-targeted observations in comparison with other methods (Qin and Mu, 2011). The CNOP method may also be applicable for studying the interactions

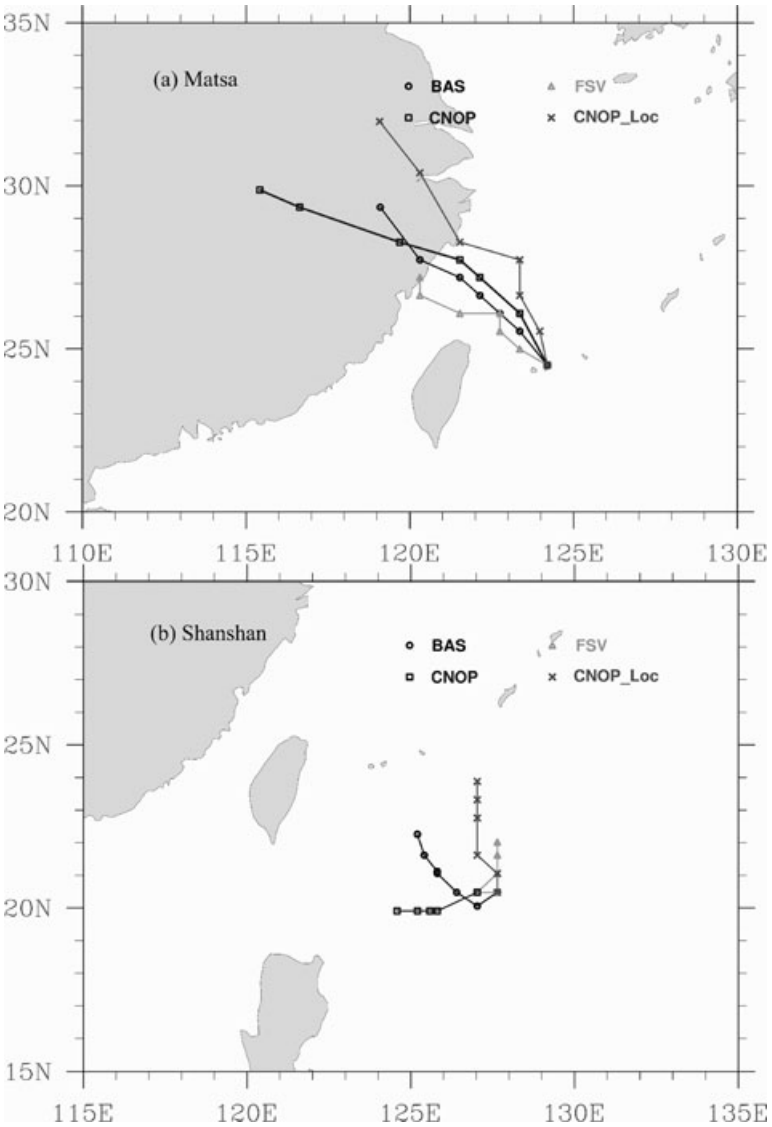

Fig. 17. The simulated tracks in the basic trajectories (BAS, same to BAS in Fig. 1) and simulated tracks with CNOP, FSV and local CNOP (CNOP_Loc) imposed on the initial condition of BAS. (a) Matsa and \ cdot (b) Shanshan.

between two hurricanes or between a hurricane and other weather systems.

Acknowledgments

We thank Juanzhen Sun for her helpful comments and suggestions on an earlier version of this manuscript. We are also grateful to Jo Hansen for her help in revising the English. MM is supported by the National Nature Science Foundation of China (No. 40830955). The two reviewers are also acknowledged for their helpful comments.

References

Aberson, S. D. 2003. Targeted observations to improve operational tropical cyclone track. *Mon. Weather Rev.* **131**, 1613–1628.

Aberson, S. D. and Etherton, B. J. 2006. Targeting and data assimilation studies during Hurricane Humberto (2001). *J. Atmos. Sci.* **63**, 175–186.

Barker, D. M., Huang, W., Guo, Y-R., Bourgeois, A. J. and Xiao, Q. N. 2004. A three-dimensional variational data assimilation system for MM5: implementation and initial results. *Mon. Weather Rev.* **132**, 897–914.

Barker, D. M., Lee, M. S., Guo, Y.-R., Huang, W., Rizvi, S. and coauthors. 2005. WRF-Var—a unified 3/4D-Var variational data assimilation system for WRF. In: *Proceedings of the Sixth WRF/15th MM5 Users' Workshop*, NCAR, Boulder, CO, 17 pp.

Birgin, E. G., Martinez, J. E. and Marcos, R. 2001. Algorithm 813: SPG—software for convex-constrained optimization. *ACM Trans. Math. Softw.* **27**, 340–349.

Bishop, C. H. and Toth, Z. 1999. Ensemble transformation and adaptive observations. *J. Atmos. Sci.* **56**, 1748–1765.

Bishop, C. H., Etherton, B. J. and Majumdar, S. J. 2001. Adaptive sampling with the ensemble transform Kalman filter. Part I: theoretical aspects. *Mon. Weather Rev.* **129**, 430–436.

Cardinali, C., Buizza, R., Kelly, G., Shapiro, M. and Thepaut, J.-N. 2007. The value of observations. Part III: influence of weather regimes on targeting. *Q. J. R. Meteorol. Soc.* **133**, 1833–1842.

Duan, W. S., Mu, M. and Wang, B. 2004. Conditional nonlinear optimal perturbations as the optimal precursors for El Niño–Southern Oscillation events. *J. Geophys. Res.* **109**, 1029–1041.

Ehrendorfer, M. and Errico, R. M. 1995. Mesoscale predictability and the spectrum of optimal perturbations. *J. Atmos. Sci.* **52**, 3475–3500.

Ehrendorfer, M., Errico, R. M. and Raeder, K. D. 1999. Singular-vector perturbation growth in a primitive equation model with moist physics. *J. Atmos. Sci.* **56**, 1627–1648.

Errico, R. M. 1985. Spectra computed from a limited area grid. *Mon. Weather Rev.* **113**, 1554–1562.

Grell, G. A., Dudhia, J. and Stauffer, D. R. 1995. A description of the fifth generation Penn State/NCAR Mesoscale Model (MM5). NCAR Tech. Note NCAR/TN-398+STR, 122 pp.

Gustafsson, N. and Huang, X.-Y. 1996. Sensitivity experiments with the spectral HIRLAM and its adjoint. *Tellus* **48A**, 501–517.

Hamill, T. M. and Snyder, C. 2002. Using improved background error covariances from an ensemble Kalman filter for adaptive observations. *Mon. Weather Rev.* **130**, 1552–1572.

Hoover, B. T. and Morgan, M. C. 2010. Validation of a tropical cyclone steering response function with a barotropic adjoint model. *J. Atmos. Sci.* **67**, 1806–1816.

Hsiao, L.-F., Liou, C.-S., Yeh, T.-C., Guo, Y.-R., Chen, D.-S. and co-authors. 2010. A vortex relocation scheme for tropical cyclone initialization in Advanced Research WRF. *Mon. Weather Rev.* **138**, 3298–3315.

Huang, X.-Y., Xiao, Q. N., Barker, D. M., Zhang, X., Michalakes, J. and co-authors. 2009. Four-dimensional variational data assimilation for WRF: formulation and preliminary results. *Mon. Weather Rev.* **137**, 299–314.

Jiang, Z. N. and Mu, M. 2009. A comparison study of the methods of conditional nonlinear optimal perturbations and singular vectors in ensemble prediction. *Adv. Atmos. Sci.* **26**, 465–470.

Langland R. H. 2005. Issues in targeted observing. *Q. J. R. Meteorol. Soc.* **131**, 3409–3425.

Langland, R. H. and Rohaly, G. D. 1996. Analysis error and adjoint sensitivity in prediction of a North Atlantic frontal cyclone. In: *Proceedings of the 11th Conf. on Numerical Weather Prediction,* Preprints, Amer. Meteor. Soc. 150–152.

Lorenz, E. N. and Emanuel, K. A. 1998. Optimal sites for supplementary weather observations: simulation with a small model. *J. Atmos. Sci.* **55**, 399–414.

Majumdar, S. J., Aberson, S. D., Bishop, C. H., Buizza, R., Peng, M. S. and co-authors. 2006. A comparison of adaptive observing guidance for Atlantic tropical cyclones. *Mon. Weather Rev.* **134**, 2354–2372.

Montani, A., Thorpe, A. J., Buizza, R. and Unden, P. 2006. Forecast skill of the ECMWF model using targeted observations during FASTEX. *Q. J. R. Meteorol. Soc.* **125**, 3219–3240.

Mu, M. and Duan, W. S. 2003. A new approach to studying ENSO predictability: conditional nonlinear optimal perturbation. *Chin. Sci. Bull.* **48**, 1045–1047.

Mu, M. and Zhang, Z. Y. 2006. Conditional nonlinear optimal perturbations of a two-dimensional quasigeostrophic model. *J. Atmos. Sci.* **63**, 1587–1604.

Mu, M., Wang, H. L. and Zhou, F. F. 2007. Application of conditional optimal perturbation to adaptive observation: preliminary results. *Chin. J. Atmos. Sci.* **31**, 1102–1112.

Mu, M., Zhou, F. F. and Wang, H. L. 2009. A method for identifying the sensitive areas in targeted observations for tropical cyclone prediction: conditional nonlinear optimal perturbation. *Mon. Weather Rev.* **137**, 1623–1639.

Palmer, T. N., Gelaro, R., Barameijer, J. and Buizza, R. 1998. Singular vectors, metrics, and adaptive observations. *J. Atmos. Sci.* **55**, 633–653.

Parrish, D. F. and Derber, J. C. 1992. The National Meteorological Center's spectral statistical-interpolation analysis system. *Mon. Weather Rev.* **120**, 1747–1763.

Pu, Z. X. and Kalnay, E. 1999. Targeting observations with the quasi-linear inverse and adjoint NCEP global models: performance during FASTEX. *Q. J. R. Meteorol. Soc.* **125**, 3329–3337.

Qin, Q. H. and Mu, M. 2011. A study on the reduction of forecast error variance by three adaptive observation approaches for tropical cyclone prediction. *Mon. Weather Rev.* **139**, 2218–2232.

Rabier, F., Klinker, E., Courtier, P. and Hollingsworth, A. 1996. Sensitivity of forecast errors to initial conditions. *Q. J. R. Meteorol. Soc.* **122**, 121–150.

Reynolds, C. A., Peng, M. S., Majumdar, S. J., Aberson, S. D., Bishop, C. H. and co-authors. 2007. Interpretation of adaptive observing guidance for Atlantic tropical cyclones. *Mon. Weather Rev.* **135**, 4006–4029.

Skamarock, W. C., Klemp, J. B., Dudhia, J., Gill, D. O., Barker, D. M., and co-authors. 2008. A description of the advanced research WRF version 3. NCAR Tech. Note TN-475+STR, 113 pp.

Wang, H. L., Sun J. Z., Guo Y.-R. and Huang X.-Y. 2011. Radar reflectivity assimilation with the four-dimensional variational system of the Weather Research and Forecast Model. In: *Proceedings of the 91st American Meteorological Society Annual Meeting*. Seattle, WA. Available at: http://ams.confex.com/ams/91Annual/webprogram/Manuscript/Paper185272/4DVAR_RF_AMS2011_Wang.pdf. Accessed on 23-27 January 2011.

Wu, C. C., Chen, J. H. and Lin, P. H. 2007a. The impact of dropwindsonde data on typhoon track forecasts in DOTSTAR. *Weather Forecast.* **22**, 1157–1176.

Wu, C. C., Chen, J. H., Lin, P. H. and Chou, K. H. 2007b. Targeted observations of tropical cyclone movement based on the adjoint-derived sensitivity steering vector. *J. Atmos. Sci.* **64**, 2611–2626.

Wu, C. C., Chen, J. H., Majumdar, S. J., Peng, M. S., Reynolds, C. A. and co-authors. 2009a. Intercomparison of targeted observation guidance for tropical cyclones in the northwestern Pacific. *Mon. Weather Rev.* **137**, 2471–2492.

Wu, C. C., Chen, S.-G., Chen, J. H., Chou, K.-H. and Lin, P.-H. 2009b. Interaction of typhoon Shanshan (2006) with the midlatitude trough from both adjoint-derived sensitivity steering vector and potential vorticity perspectives. *Mon. Weather Rev.* **137**, 852–862.

Xiao, Q. N., Kuo, Y.-H., Ma, Z. Z., Huang, W., Huang, X.-Y., and co-authors. 2008. Development of the WRF adjoint modeling system and its application to the investigation of the May 2004 McMurdo Antarctica severe wind event. *Mon. Weather Rev.* **136**, 3696–3713.

Zhang, M., Zhang F. Q., Huang X.-Y. and Zhang X. 2010. Intercomparison of an ensemble Kalman filter with three- and four-dimensional variational data assimilation methods in a limited-area model over the month of June 2003. *Mon. Weather Rev.* **139**, 566–572.

Zhou F. F. and Mu M. 2011. The impact of verification area design on tropical cyclone targeted observations based on the CNOP method. *Adv. Atmos. Sci.* In press.

Zou, X. L., Vandenberghe, F., Pondeca, M. and Kuo Y.-H. 1997. Introduction to adjoint techniques and the MM5 adjoint modeling system. NCAR Technical Note, NCAR/ TN2435 + STR, 110 pp, [Available from NCAR, P.O. Box 3000, Boulder, CO 80307-3000].